

Dissolution of Biogenic and Synthetic UO_2 under Varied Reducing Conditions

KAI-UWE ULRICH,^{*,†} ABHAS SINGH,[†]
ELEANOR J. SCHOFIELD,[‡]
JOHN R. BARGAR,[‡] HARISH VEERAMANI,[§]
JONATHAN O. SHARP,[§]
RIZLAN BERNIER-LATMANI,[§] AND
DANIEL E. GIAMMAR[†]

Department of Energy, Environmental and Chemical Engineering, Washington University, One Brookings Drive, St. Louis, Missouri 63130, Stanford Synchrotron Radiation Laboratory, SLAC, 2575 Sand Hill Road, Menlo Park, California 94025, and Ecole Polytechnique Fédérale de Lausanne, CH-1015 Lausanne, Switzerland

Received March 4, 2008. Revised manuscript received April 16, 2008. Accepted April 21, 2008.

The chemical stability of biogenic UO_2 , a nanoparticulate product of environmental bioremediation, may be impacted by the particles' surface free energy, structural defects, and compositional variability in analogy to abiotic UO_{2+x} ($0 \leq x \leq 0.25$). This study quantifies and compares intrinsic solubility and dissolution rate constants of biogenic nano- UO_2 and synthetic bulk $\text{UO}_{2.00}$, taking molecular-scale structure into account. Rates were determined under anoxic conditions as a function of pH and dissolved inorganic carbon in continuous-flow experiments. The dissolution rates of biogenic and synthetic UO_2 solids were lowest at near neutral pH and increased with decreasing pH. Similar surface area-normalized rates of biogenic and synthetic UO_2 suggest comparable reactive surface site densities. This finding is consistent with the identified structural homology of biogenic UO_2 and stoichiometric $\text{UO}_{2.00}$. Compared to carbonate-free anoxic conditions, dissolved inorganic carbon accelerated the dissolution rate of biogenic UO_2 by 3 orders of magnitude. This phenomenon suggests continuous surface oxidation of U(IV) to U(VI), with detachment of U(VI) as the rate-determining step in dissolution. Although reducing conditions were maintained throughout the experiments, the UO_2 surface can be oxidized by water and radiogenic oxidants. Even in anoxic aquifers, UO_2 dissolution may be controlled by surface U(VI) rather than U(IV) phases.

Introduction

The remediation of uranium-contaminated soils and groundwater is an environmental challenge worldwide. Because uraninite (nominally UO_2) is stable over geological time spans in low-temperature geological and sedimentary environments (1, 2), the formation of UO_2 in the ground has been proposed to immobilize U contamination *in situ*. Dissimilatory metal- and sulfate-reducing bacteria can couple the

reduction of dissolved U(VI) to the oxidation of organic matter and H_2 , resulting in the precipitation of biogenic UO_2 (bio- UO_2) (3–5). The stimulation of such bacteria has been tested for subsurface remediation of U-contaminated aquifers and sediments (6–8).

Bioremediation can be successful if dissolution and/or reoxidation of bio- UO_2 are slow enough to keep dissolved U concentrations below regulatory threshold values, such as the U.S. EPA drinking water standard of $30 \mu\text{g/L}$ (9). However, recent studies on the remobilization of U after microbial reduction of U(VI) in soils and sediments have reported oxidation-driven U release on time-scales of six hours to several weeks (10, 11). Oxidation of U(IV) was even observed in field sediments that included microbes capable of U(VI) reduction (12). Because these studies investigated complex media, thermodynamic and kinetic properties of bio- UO_2 solids are unknown. Spectroscopic data have recently been used to estimate lattice contraction and surface stress of bio- UO_2 nanoparticles, predicting a 10^9 -fold increase in solubility compared to crystalline uraninite (13). Such a dramatic change in stability would render bio- UO_2 a relatively poor sink phase even under reducing conditions. Thus, fundamental knowledge on the key properties predicting the stability of bio- UO_2 nanoparticles is required.

The objectives of this study are to characterize intrinsic solubility and dissolution kinetics of bio- UO_2 nanoparticles under reducing conditions, where UO_2 materials are expected to be most stable. Dissolution rates of bio- UO_2 and its synthetic analog are determined in the absence and presence of inorganic carbon and as a function of pH. To elucidate the impact of particle size, structure, and stoichiometry on intrinsic properties and dissolution mechanisms of bio- UO_2 , relevant results of detailed structural studies (14) are also presented.

Experimental Section

Materials. All reagents used in this study were certified analytical grade or better. The preparation of UO_2 materials and all aliquot transfer actions took place in an anaerobic chamber (Coy Laboratory Products Inc.) containing a gas mixture of 95 vol% $\text{N}_{2(\text{g})}$ and 5 vol% $\text{H}_{2(\text{g})}$ that was circulated through a Pd catalyst and silica gel. The $\text{O}_{2(\text{g})}$ fugacity was monitored by a Coy sensor and maintained below the detection limit of 10^{-6} bar (1 ppm), representing an $\text{O}_{2(\text{aq})}$ equilibrium concentration of $<10^{-8.9}$ M. The preparation protocols for synthetic uraninite (syn- UO_2) and bio- UO_2 are given in the Supporting Information (SI). In brief, syn- UO_2 powder was produced by chemical reduction of stutite ($\text{UO}_2\text{O}_2 \cdot 4\text{H}_2\text{O}_{(\text{s})}$) with heated $\text{H}_{2(\text{g})}$. Bio- UO_2 was gained from enzymatic reduction of uranyl carbonate coupled to lactate oxidation under anaerobic conditions both at pH 6.3 and 8.0 using *Shewanella oneidensis* strain MR-1. The resulting bio- UO_2 solid was isolated from the biomass after treatment involving sonication and lysozyme or 1 M NaOH. The NaOH-treated material was used in this study unless otherwise noted. A reference sample of stoichiometric syn- $\text{UO}_{2.00}$ was provided courtesy of David Clark at Los Alamos National Laboratory (cf. Table 1 for nomenclature of study materials).

Dissolution Experiments. UO_2 dissolution under continuous flow prevents accumulation of dissolved U and maintains undersaturated conditions in a continuous-flow reactor (CFR). A detailed description of the setup is given in the SI (Figure S1). Custom-made CFRs of 12.58 mL volume were magnetically stirred and operated in the dark at room temperature (20 ± 1 °C). Influent flow rates were set between 0.2 and 2.1 mL/min and gravimetrically monitored based on effluent volume. These

* Corresponding author phone: 314-935-6234; fax: 314-935-7211; e-mail: k.ulrich@seas.wustl.edu.

[†] Washington University in St. Louis.

[‡] Stanford Synchrotron Radiation Laboratory.

[§] Ecole Polytechnique Fédérale de Lausanne.

TABLE 1. Summary of UO₂ Synthesis and Main Characteristics of the Study Materials

UO ₂ material	biogenic		abiotic	
	oxidant	U(VI) _(aq) , mainly UO ₂ (CO ₃) ₃ ⁴⁻		solid studtite (UO ₂ O ₂ ·4H ₂ O)
reductant	<i>Shewanella oneidensis</i> MR1		H _{2(g)} at 400 °C	
pH of U(VI) reduction	6.3	8.0		
Sample ID	bio6-UO₂	bio8-UO₂	synA-UO₂^a	synB-UO₂
specific surface area (m ² /g)	50.14 ^b		5.93 ^b	3.1 ^c
crystallite size range (nm)	1.5 – 3.5 ^d		92 – 200 ^e	600 – 800 ^f

^a Courtesy of Dan Schwarz and David Clark, Los Alamos National Laboratory. ^b Multipoint N₂-BET. ^c Calculated from particle morphology visualized by scanning electron microscopy (SEM). ^d Derived from high-resolution transmission electron microscopy (HR-TEM) and synchrotron-based powder diffraction (SR-PD). ^e Lower value calculated from SSA, higher value taken from SEM images (upper limit). ^f Based on SEM images.

flow rates were chosen to provide short residence times to keep the H₂ level in the CFR high enough to sustain a reducing environment and to achieve steady-state effluent dissolved U concentrations far below saturation (15). The influent [O₂]_{diss} was monitored by a dissolved oxygen sensor (Microelectrodes, Inc.), and the U-concentration was periodically measured to establish that the feed solution, tubing, and reactor materials released negligible uranium. The effluent passed through 0.2 μm (polycarbonate) or 0.025 μm (mixed cellulose ester, both Millipore) filter membranes at the CFR exit and was continuously collected for pH measurement and U analyses.

The UO₂ dissolution was studied at chemical conditions relevant to groundwater remediation. Reducing conditions were equilibrated in the feed solution by bubbling a mixture of 95 vol% N₂ and 5 vol% H₂ in presence of a Pd catalyst. The first step in all experiments used an influent at near neutral pH (stabilized with HEPES or TAPS organic buffer) that was applied for up to 40 residence times. In selected experiments, the continuous flow was then stopped and reactors were run in batch mode for 4 d to determine the difference between the steady-state, [U]_{ss}, and equilibrium, [U]_{eq}, concentrations. In other experiments, further continuous-flow steps provided either 1 mM anoxic NaHCO₃ or NaCl and diluted HCl in the feed solution. Because the solid concentration of the bio-UO₂ suspensions was initially unknown, the residual UO₂ solid was digested in strong acid and analyzed for total U.

Analysis. The total U concentrations of the residual solids, the influent, [U]_{in}, and the effluent were determined in a 0.1 M HNO₃ matrix by ICP-MS (Agilent 7500ce) with a detection limit of <10 ng/L. The dissolved U(VI) concentration was spectrophotometrically determined in selected samples using the Bromo-PADAP method (16) with a detection limit of ~0.1 μM. The syn-UO₂ material was analyzed by XRD (Rigaku D-MAX/A) using Cu Kα radiation, and imaged by scanning electron microscopy (Hitachi S-4500) of Au-coated UO₂ particles dispersed directly on sample mounts or loaded on pieces of filters. U L_{III}-edge X-ray absorption data on syn-UO₂ and bio-UO₂ were collected at SSRL beamlines 10-2 and 11-2 equipped with a Si(220) double-crystal monochromator which was calibrated by using yttrium foil. Extended X-ray absorption fine structure (EXAFS) spectra were background subtracted, splined, and analyzed using SIXPack (17) with FEFF8 backscattering phase and amplitude functions (18). *In-situ* synchrotron powder diffraction (SR-PD) data were collected in transmission geometry on SSRL beamline 7-2. The incident X-ray beam was set to 16.1 keV (λ = 0.77 Å) and the diffractometer was calibrated with LaB₆. Wet samples were loaded into quartz capillaries. Data were collected in Q-space of 0.02 Å⁻¹ intervals out to ~14.5 Å⁻¹. Multiple scans were taken and averaged in order to improve the signal-to-noise ratio.

Dissolution Rate Calculation. The dissolution rate of UO₂ solid loaded into a CFR can be calculated from the mass

balance equation (eq 1) once steady-state is reached, i.e., $d[U]_{\text{eff}}/dt = 0$. This takes at least 5 residence times, $\tau = VQ^{-1}$ (min).

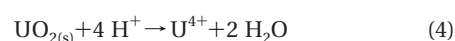
$$V \times \frac{d[U]_{\text{eff}}}{dt} = Q \times [U]_{\text{in}} - Q \times [U]_{\text{eff}} + V \times R_d \quad (1)$$

In eq 1 [U]_{eff} and [U]_{in} (mol L⁻¹) are the U concentrations in the effluent and influent, V (L) is the reactor volume, Q (L min⁻¹) is the flow rate, and R_d (mol L⁻¹ min⁻¹) is the rate of U release to solution from UO₂ dissolution. Assuming [U]_{in} is zero, the dissolution rate can be calculated as follows:

$$R_m = \frac{Q \times [U]_{\text{ss}}}{V \times [\text{solid}]} \quad (2)$$

$$R_n = \frac{Q \times [U]_{\text{ss}}}{V \times \text{SSA} \times [\text{solid}]} \quad (3)$$

where R_m (mol g⁻¹ min⁻¹) and R_n (mol m⁻² min⁻¹) are the dissolution rates normalized to mass and specific surface area, SSA (m² g⁻¹), respectively, and [solid] (g L⁻¹) is the mass concentration of UO₂ in the reactor. The rate calculation accounts for the changes in [solid] and SSA with time that result from UO₂ dissolution (see SI for details). The reaction rate constant, k (mol m⁻² min⁻¹), in a general rate equation that accounts for the reaction affinity (i.e., distance to equilibrium with respect to eq 4) can be derived from eq 5.



$$R_n = k \times \text{SSA} \times [\text{solid}] \left(1 - \frac{[\text{U}^{4+}]_{\text{eff}}[\text{H}^+]_{\text{eff}}}{K_{\text{sp,UO}_2}} \right) = k \times \text{SSA} \times [\text{solid}] \times \left(1 - \frac{[\text{U}]_{\text{eff}}}{[\text{U}]_{\text{eq}}} \right) \quad (5)$$

Calculation of [U]_{eq} is based on thermodynamic data given in Table S1 in the SI. A numerical solution to predict [U]_{eff}, [solid], and SSA as a function of time was developed and used to determine optimal values of k (see SI for details).

Results and Discussion

Structural Properties. The synthetic UO₂ materials were brown or blackish brown powders consisting of a highly crystalline face-centered cubic lattice as identified by powder XRD (Figure S3, SI). The synthetic UO₂ particle morphology and size were visualized by SEM (Figure S2, SI). Particles had mean diameters of about 100–200 nm (synA-UO₂) or 600–800 nm (synB-UO₂). Bio-UO₂ particles had diameters of 1.5–3.5 nm as determined by Fourier filtered HR-TEM images (14). Multipoint N₂-BET measured a SSA of 50.14 m² g⁻¹ for bio-UO₂ and 5.93 m² g⁻¹ for synA-UO₂. A mean SSA of 3.1 m² g⁻¹ was calculated for synB-UO₂ from the morphology of the particles observed by SEM. This number is likely to represent

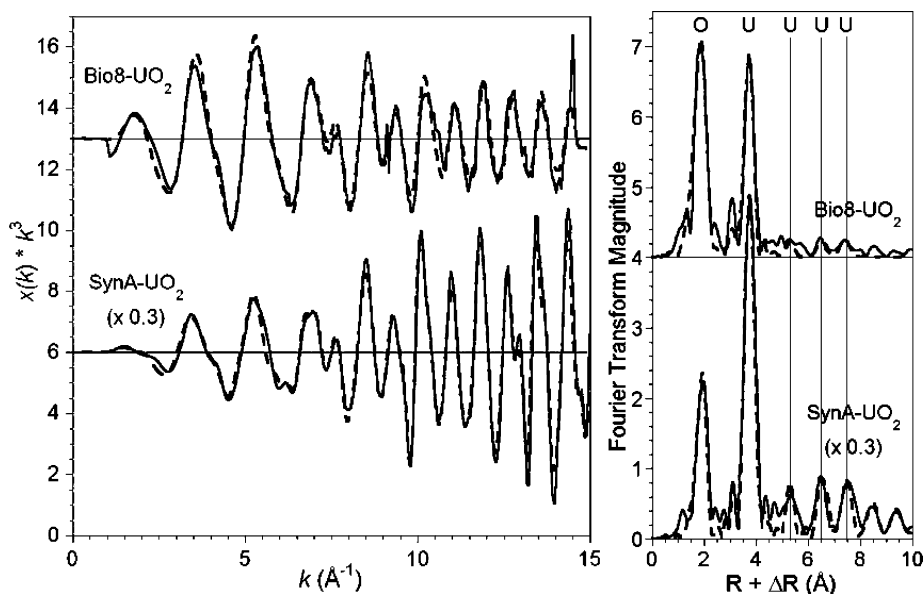


FIGURE 1. (a) Uranium L_3 edge EXAFS spectra (k^3 weighted) and (b) Fourier transform magnitude of bio8- UO_2 and synA- $\text{UO}_{2.00}$. Solid lines show experimental data, dashed lines represent the fit of structural data. Neighbor O- and U-shells appear at similar radial distance up to 8 Å ($R + \Delta R$) in both materials, and are visible beyond 8 Å in $\text{UO}_{2.00}$.

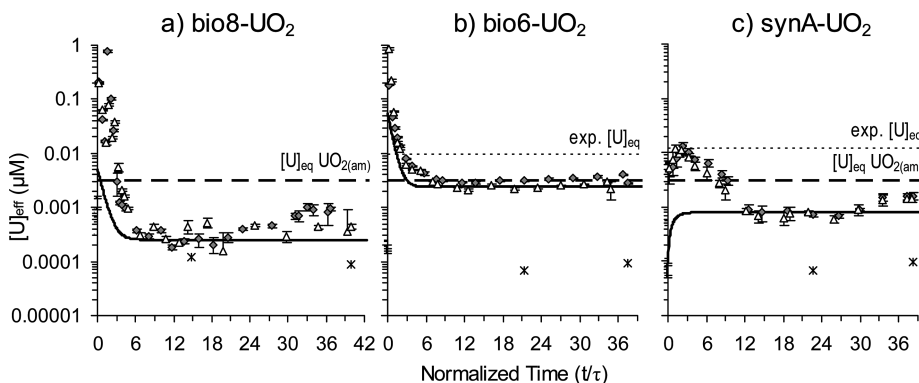


FIGURE 2. Dissolution of (a) bio8- UO_2 , (b) bio6- UO_2 , and (c) synA- UO_2 under reducing, carbonate-free conditions ($\text{pH } 7.5 \pm 0.2$). Triangles and diamonds represent effluent concentrations of dissolved U of two replicate reactors as a function of normalized time ($\tau \sim 6$ min). Error bars reflecting analytical standard deviation are mostly smaller than the symbol size. Stars show the U background concentration in the influent. The dotted and dashed lines indicate the equilibrium concentration, $[\text{U}]_{\text{eq}}$, determined experimentally and calculated from thermodynamics of a so-called amorphous UO_2 phase, respectively (cf. SI, Figure S5). The solid line illustrates the predicted response to the initial U load assuming a dissolution rate constant of (a) 1.0×10^{-14} , (b) 5.5×10^{-13} , and (c) $3.3 \times 10^{-13} \text{ mol U m}^{-2} \text{ s}^{-1}$.

a lower estimate because it does not account for surface roughness. *In-situ* SR-PD indicated lattice constants of 5.467 and 5.460 Å for lysozyme-treated bio8- UO_2 and bio6- UO_2 , respectively, consistent with stoichiometric $\text{UO}_{2.00}$. After the treatment with NaOH solution, the unit cell constant diminished to 5.444 and 5.430 Å, indicating compression of the particles, presumably due to hydroxylation of the surface. SR-PD peak-fitting suggests a crystallite size of ~ 3.5 nm. The EXAFS oscillations and Fourier transforms of untreated bio8- UO_2 and synA- UO_2 show that U–U single scattering shells are present up to a distance of 8 and 10 Å ($R + \Delta R$), respectively. Albeit the intermediate-range order of the NaOH-treated bio- UO_2 materials appears weaker, the structures are consistent with that of stoichiometric $\text{UO}_{2.00}$ (Figure 1). Furthermore, the U–O shell distances of bio8- UO_2 (2.347 Å), bio6- UO_2 (2.336 Å), and syn- $\text{UO}_{2.00}$ (2.347 Å) are not distinguishable within the experimental error (14). There is no evidence for splitting of the U–O shell, as would be expected for UO_{2+x} ($x > 0$). These observations support a general structural homology between the bio- UO_2 samples and stoichiometric $\text{UO}_{2.00}$. The lack of U–U shells beyond 8 Å is attributed to a loss of long-range order in the nano-

particles beyond this distance. Details of the synchrotron-based structural characterization of bio- UO_2 are presented elsewhere (14).

Dissolution at Neutral pH Conditions. Dissolution rates of two biogenic and two synthetic UO_2 materials (Table 1) were determined from duplicate continuous flow experiments carried out in the absence of dissolved inorganic carbon (DIC) under reducing conditions at near neutral pH (7.2–8.0). The replicate results were in excellent agreement (Figure 2). Bio8- UO_2 and synA- UO_2 reached $[\text{U}]_{\text{ss}}$ of the same order of magnitude (0.2–0.8 nM). The $[\text{U}]_{\text{ss}}$ of bio6- UO_2 and synB- UO_2 (not shown) were about 1 order of magnitude higher. The mass-based dissolution rates of bio- UO_2 and syn- UO_2 ranged from 5×10^{-13} to $2 \times 10^{-11} \text{ mol U g}^{-1} \text{ s}^{-1}$ (Table 2), spanning more than 2 orders of magnitude. When normalized to surface area, lower rates were found for the bio- UO_2 solids (1.1×10^{-14} to $3.4 \times 10^{-13} \text{ mol U m}^{-2} \text{ s}^{-1}$) than for the syn- UO_2 solids (2.8×10^{-13} to $2.1 \times 10^{-12} \text{ mol U m}^{-2} \text{ s}^{-1}$). The data of R_n (eq 3) are consistent with published dissolution rates of synthetic UO_2 materials (7.5×10^{-13} to $4.2 \times 10^{-12} \text{ mol U m}^{-2} \text{ s}^{-1}$, Table 2). Because the measured equilibrium solubility of bio6- UO_2 (9.5 nM) and synA- UO_2

TABLE 2. Comparison of UO_2 Dissolution Rates Measured under Reducing, Carbonate-Free Conditions (R_m and R_n are means Calculated by eqs 2 and 3; the Rate Constant k is Obtained from the Dissolution Model (eq 5) Assuming Steady-State Was Reached; All Rates Account for the Time-Dependent Loss of Solid while Dissolution)

UO_2 material	experimental				R_m mol g^{-1} s^{-1}	R_n mol m^{-2} s^{-1}	k mol m^{-2} s^{-1}	ref ^b
	SSA (m^2/g)	[solid] (g/L)	pH	influent electrolyte				
bio6- UO_2	50.14	1.15	7.60	1 mM HEPES	$4.94 \cdot 10^{-12}$	$9.85 \cdot 10^{-14}$	$2.50 \cdot 10^{-13}$	
bio6- UO_2	50.14	0.47	7.25	1 mM HEPES	$1.71 \cdot 10^{-11}$	$3.42 \cdot 10^{-13}$	$4.75 \cdot 10^{-13}$	
bio8- UO_2	50.14	1.60	7.67	1 mM HEPES	$5.35 \cdot 10^{-13}$	$1.07 \cdot 10^{-14}$	$1.17 \cdot 10^{-14}$	
bio8- UO_2	50.14	1.65	4.15	1 mM NaCl	$1.37 \cdot 10^{-08}$	$2.69 \cdot 10^{-10}$	N/A	
bio8- UO_2	50.14	1.56	3.10	1 mM HCl	$2.75 \cdot 10^{-08}$	$5.25 \cdot 10^{-10}$	N/A	
bio8- UO_2	50.14	1.40	2.15	10 mM HCl	$2.12 \cdot 10^{-08}$	$3.92 \cdot 10^{-10}$	$4.00 \cdot 10^{-10}$	
synB- UO_2	3.10	0.82	8.00	1 mM NaNO_3 , TAPS	$1.25 \cdot 10^{-11}$	$4.03 \cdot 10^{-12}$	$1.33 \cdot 10^{-11}$	
synA- UO_2	5.93	0.79	7.70	1 mM HEPES	$3.27 \cdot 10^{-12}$	$5.51 \cdot 10^{-13}$	$8.75 \cdot 10^{-13}$	
synA- UO_2	5.93	1.25	7.25	1 mM HEPES	$1.66 \cdot 10^{-12}$	$2.80 \cdot 10^{-13}$	$3.17 \cdot 10^{-13}$	
synA- UO_2	5.93	1.35	5.20	1 mM NaCl	$3.27 \cdot 10^{-10}$	$5.52 \cdot 10^{-11}$	N/A	
synA- UO_2	5.93	1.35	4.10	1 mM NaCl	$8.32 \cdot 10^{-10}$	$1.40 \cdot 10^{-10}$	N/A	
synA- UO_2	5.93	1.33	3.10	1 mM HCl	$4.05 \cdot 10^{-09}$	$6.78 \cdot 10^{-10}$	$1.67 \cdot 10^{-09}$	
synA- UO_2	5.93	1.13	2.10	10 mM HCl	$3.85 \cdot 10^{-09}$	$6.38 \cdot 10^{-10}$	$6.67 \cdot 10^{-10}$	
published dissolution rates obtained from CFR experiments on abiotic UO_2								
syn- $\text{UO}_{2.001}$	0.201	0.5 g ^a	6.65	8 mM NaClO_4		$4.18 \cdot 10^{-12}$		(29)
syn- $\text{UO}_{2.001}$	0.201	0.5 g ^a	7–11	8 mM NaClO_4		$1.90 \cdot 10^{-12}$		(29)
syn- UO_2	3.94	1.0	7.5	10 mM NaClO_4		$7.50 \cdot 10^{-13}$		(34)
SNF grains	0.03	230	5.8	10 mM NaCl		$1.46 \cdot 10^{-13}$		(15)

^a A thin film of 0.5 g $\text{UO}_{2.0}$ was used in this work. ^b If no reference given, data are from the present work.

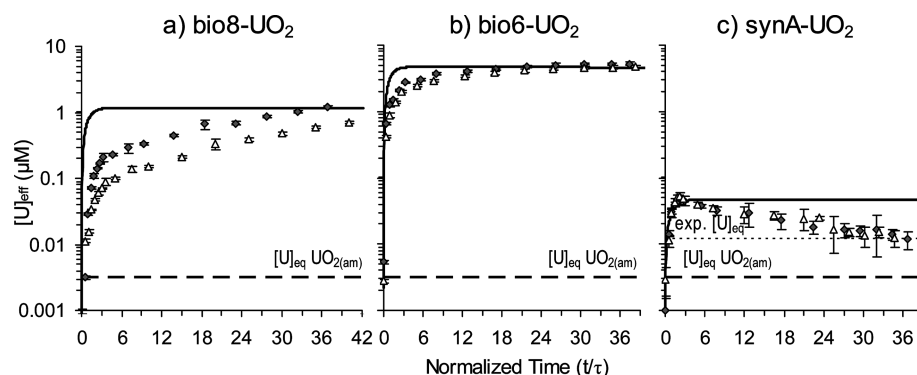


FIGURE 3. Dissolution of (a) bio8- UO_2 , (b) bio6- UO_2 , and (c) synA- UO_2 under reducing conditions in presence of 1 mM DIC (pH 8.1 ± 0.3). Triangles and diamonds represent effluent concentrations of dissolved U of two replicate reactors as a function of normalized time ($\tau \sim 6\text{--}9$ min). Error bars reflecting analytical standard deviation are mostly smaller than the symbol size. UO_2 dissolution was continued from the experiment shown in Figure 2. The dotted and dashed lines indicate the equilibrium concentration determined experimentally and calculated from thermodynamic data, respectively (cf. SI, Figure S5). In a U(VI) containing system, $[\text{U}]_{\text{eq}}$ of schoepite is predicted at 20–40 μM depending on pH and [DIC]. The solid line illustrates the predicted response to UO_2 dissolution with a rate constant of (a) 4.0×10^{-11} , (b) 1.75×10^{-10} , and (c) 2.7×10^{-11} mol U m^{-2} s^{-1} .

(12 nM) was relatively close to $[\text{U}]_{\text{ss}}$ (Figure 2b and c), the reaction affinity must be considered when calculating intrinsic rate constants (k) for UO_2 dissolution. These values range from 1.2×10^{-14} to 4.8×10^{-13} mol U m^{-2} s^{-1} for the two bio- UO_2 materials, and from 3.2×10^{-13} to 1.3×10^{-11} mol U m^{-2} s^{-1} for the two syn- UO_2 materials.

The $[\text{U}]_{\text{eq}}$ obtained for bio6- UO_2 and synA- UO_2 was very similar, although the particle sizes of these two materials were quite different (Table 1). This similarity in equilibrium solubility is in accordance with the structural homology between bio- UO_2 and $\text{UO}_{2.00}$ as determined by EXAFS and SR-PD (14), and suggests a minor impact of surface free energy on the solubility of nanoparticulate bio- UO_2 in water. The measured $[\text{U}]_{\text{eq}}$ values are slightly higher than those calculated from the NEA thermodynamic database considering $\text{UO}_{2(\text{am})}$ (19). The solubility of $\text{UO}_{2(\text{am})}$ was chosen as a reference and depicted in Figures 2 to 4 because this data is consistent with the best experimental solubility measurements carried out in aqueous solution at extremely low O_2 fugacity $< 10^{-65}$ atm (20). The present paper will not address the intrinsic solubility of $\text{UO}_{2(\text{cr})}$ in water, which is still a matter of debate (21, 22).

All experiments showed an initial $[\text{U}]_{\text{eff}}$ peak immediately after the onset of UO_2 dissolution, which was higher for the bio- UO_2 materials ($\sim 1 \mu\text{M}$) than for the syn- UO_2 materials ($\sim 0.02 \mu\text{M}$). Such a transient pulse release of U is a common phenomenon of flow-through experiments and has been attributed to labile U(VI) on the UO_2 surface (23–25). The higher $[\text{U}]_{\text{eff}}$ peak for bio- UO_2 than syn- UO_2 is consistent with a greater surface area allowing more accumulation of U(VI) on the surface. Another possible explanation for the $[\text{U}]_{\text{eff}}$ peak is passage of colloidal UO_2 through the filter membrane during the first flush.

Carbonate Promoted Dissolution. The presence of carbonate is not expected to significantly alter the solubility of $\text{UO}_{2(\text{am})}$ in an anoxic system. For example, upon the addition of 1 mM inorganic carbon, the dissolved [U] would only increase from 3.16 to 3.24 nM (between pH 7.3 and 7.6) from the formation of aqueous U(IV)-carbonate complexes (19) (Figures S5 and S6, SI). However, if U(VI) is present, highly soluble U(VI) carbonate complexes will form (Figure S6b). Thus, if carbonate addition under reducing conditions

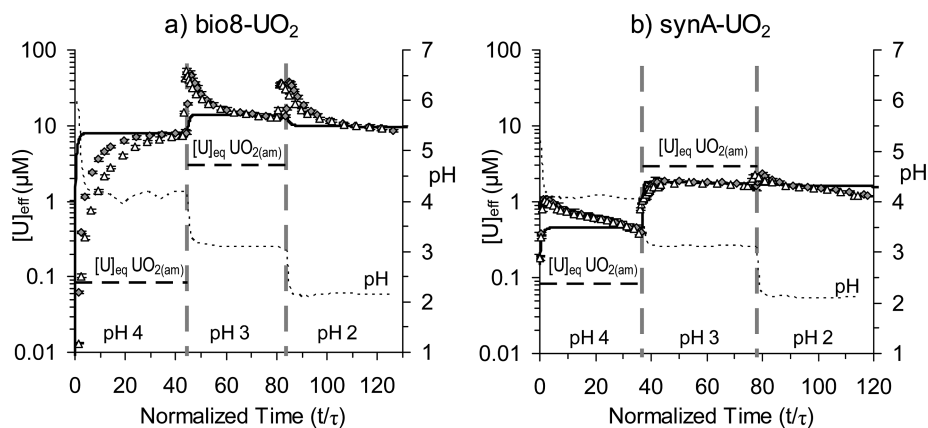


FIGURE 4. Dissolution of (a) bio8-UO₂ and (b) synA-UO₂ under reducing conditions at three consecutive pH levels. Triangles and diamonds represent effluent concentrations of dissolved U of two replicate reactors as a function of normalized time ($\tau \sim 6$ min). Error bars reflecting analytical standard deviation are mostly smaller than the symbol size. The dotted line represents the effluent pH based on the right ordinate. UO₂ dissolution was continued from anoxic dissolution at near neutral pH (bio8-UO₂) or pH 5 (synA-UO₂). The vertical dashed lines indicate the switch of influent pH, the horizontal dashed lines show the equilibrium concentration calculated for UO_{2(am)} (cf. SI). At pH 2.2, [U]_{eq} of UO_{2(am)} is 263 μ M, exceeding the limit of the left y-axis. The solid line illustrates the predicted response to UO₂ dissolution at rate constants of 2.8×10^{-10} , 5.3×10^{-10} , and 4.0×10^{-10} mol U m⁻² s⁻¹ for bio8-UO₂, and 1.5×10^{-10} , 1.7×10^{-9} , and 6.7×10^{-10} mol U m⁻² s⁻¹ for synA-UO₂, at pH 4, pH 3, and pH 2, respectively.

leads to a higher UO₂ dissolution rate, U(VI) must have continuously formed on the UO₂ surface by oxidation.

All tested UO₂ materials showed clear evidence of carbonate-induced U release (Figure 3). The increase in [U]_{eff} upon the addition of carbonate spanned 2–3 orders of magnitude and was higher for the bio-UO₂ than for the synA-UO₂ material. For the latter, the step function increase in dissolution rate to 2.7×10^{-11} mol U m⁻² s⁻¹ was followed by a slowly declining net rate, with the [U]_{eff} approaching the same [U]_{eq} as determined earlier in carbonate-free solution (Figure 3c). This suggests that the detachment of U(VI) from the surface was faster than U(IV) oxidation, limiting the replenishment of U(VI) ions on the UO₂ surface. A similar dissolution pattern was observed for spent fuel in H_{2(g)} saturated solution containing 10 mM NaHCO₃ (15). These results suggest that surface U(IV) oxidation occurred in the absence of carbonate, i.e., during the previous condition, and that UO₂ dissolution is controlled by a surface layer of U(VI) that accumulates over time and protects underlying U(IV) atoms from oxidation. According to the standard redox potential of U(VI)/U(IV) and H⁺/H_{2(aq)}, U(IV) oxidation is thermodynamically favorable in pH 7 water up to a concentration of ~ 7 nM dissolved U(VI) (19). Low but significant concentrations of dissolved H_{2O₂} and O₂ on the order of 10⁻⁹ M can result from α -radiolysis of water at steady state and the given concentration of depleted U (15, 26–28). Natural U will lead to higher concentrations of oxidants due to higher concentrations of short-lived daughter products and their α/β -radiation.

In contrast to syn-UO₂, the [U]_{eff} of the bio-UO₂ materials approached or reached steady state at much higher concentrations of > 1 to 5 μ M, more than 100 times higher than that measured for synA-UO₂. For the bio-UO₂, U(IV) oxidation cannot be rate-limiting. Rather the detachment of U(VI) or the dissolution of a U(VI) coating phase similar to schoepite (UO₃·2H₂O) controls the net dissolution of bio-UO₂.

Proton Promoted Dissolution. The [U]_{eff} increased considerably when the influent pH was lowered from near neutral to pH 4, pH 3, and pH 2 under reducing conditions (Figure 4). At pH 4, [U]_{eff} of both UO₂ materials exceeded the calculated equilibrium solubility of UO_{2(am)}, with a greater difference for the bio8-UO₂ material. After switching to pH 3, [U]_{eff} of bio8-UO₂ peaked at ~ 50 μ M and declined steadily thereafter, still exceeding the calculated equilibrium solubility of UO_{2(am)}. In contrast, [U]_{eff} of synA-UO₂ responded in the predicted way to the step-function increase in UO₂ dissolution

rate, approaching [U]_{ss} of ~ 1.8 μ M, which is below the calculated equilibrium solubility of UO_{2(am)}. At pH 2, the [U]_{eff} pattern of bio8-UO₂ resembled the pattern seen at pH 3. For both UO₂ materials at pH 2, the [U]_{eff} peak was followed by a slow decrease in [U]_{eff} far below the calculated equilibrium solubility of UO_{2(am)} of 263 μ M.

An increase in UO₂ solubility is expected at acidic pH due to proton promoted hydrolysis (19). The hydrolysis reaction depends on the valence of surface bound U. Since U(VI) is likely to be formed on the UO₂ surface even under reducing conditions, hydrolysis of U(VI) rather than U(IV) is likely in cases where the equilibrium solubility of UO_{2(am)} was exceeded. This reaction was most obvious for the bio-UO₂ material, which also dissolved faster in the presence of carbonate. The idea that hydrolysis reactions enhanced the detachment of U(VI) from the UO₂ surface is supported by nearly identical U(VI) and total U concentrations analyzed in the effluent of bio8-UO₂ even at a pH as low as 3. Although specific reasons for the transient [U]_{eff} peaks are unknown, we hypothesize that rapid pH changes cause structural changes on the surface including bond breaks, and lead to instantaneous net loss of U.

Figure 5 shows the dissolution rates of synA-UO₂ and bio8-UO₂ plotted as a function of pH. The rates were highly consistent below pH 6 when normalized to surface area (Figure 5b). This implies a similar number and reactivity of sites per unit surface area. For the pH range between 3 and 8, the dissolution of synA-UO₂ can be described by a log-linear relationship (eq 6) with the standard error presented as the uncertainty.

$$R_n (\text{mol m}^{-2} \text{s}^{-1}) = 8.3 \pm 3.2 \times 10^{-8} [\text{H}^+]^{0.66 \pm 0.03} \quad (3 \leq \text{pH} \leq 8) \quad (6)$$

A similar relationship was reported for proton promoted dissolution of synthetic UO₂ at reducing conditions, with R_n (mol m⁻² s⁻¹) = $1.4(\pm 0.3) \times 10^{-8} [\text{H}^+]^{0.53 \pm 0.08}$ (29). The fractional reaction order between 0 and 1 is consistent with dissolution of other metal oxide surfaces under acidic conditions. The reaction order was found to be fractional if the dissolution rate depends on the activity of H⁺ adsorbed to the surface (30). To compare the dissolution kinetics of common soil minerals and syn-UO₂, the latter was found to dissolve at least 1 order of magnitude faster at pH 3 to 6 than biotite [KMgFe₂AlSi₃O₁₀(OH)₂] or goethite (α -FeOOH) (31).

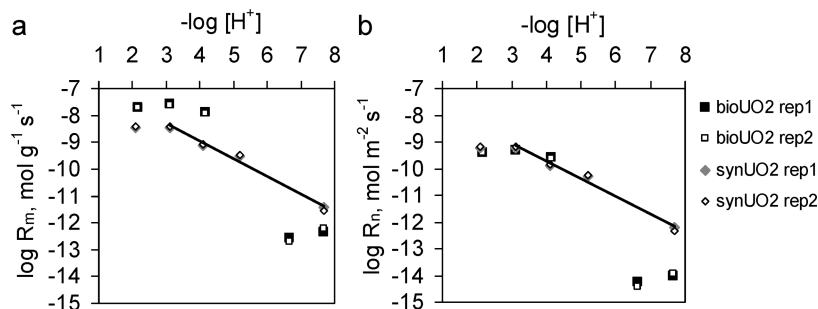


FIGURE 5. Dissolution rates of two replicates of bio8-UO₂ and synA-UO₂ solids as a function of pH under reducing conditions in the absence of carbonate. (a) Rates R_m given per unit mass and time, and (b) R_n normalized to surface area. The lines show the linear regression of synA-UO₂ dissolution rates from pH 3 to 8, which yielded a correlation coefficient (r^2) of 0.985.

Implications for Remediation. Different processes contribute to the dissolution of biogenic UO₂ in reducing environments: (i) proton attack on the UO₂ surface dissolving U(IV) aqueous species, the rate of which is a function of pH and site density, (ii) continuous oxidation of surface-exposed U(IV) to U(VI), where the rate depends on the activity of trace oxidants and accessible U(IV) sites, and (iii) detachment of surface bound U(VI) into solution, which is a function of pH and activity of complexing agents such as carbonate. The experimental data suggest that in reducing environments UO₂ dissolution is primarily controlled by the detachment of U(VI) ions. The formation of a thin surface layer of U(VI) by either adsorption or surface oxidation is generally fast and thermodynamically favorable in water. Surface oxidation can also result from trace amounts of oxidants formed by α -radiolysis of water. The presence of an outer layer of U(VI) on the UO₂ surface is consistent with structural investigations of this material that suggest the presence of short-range structural disorder in the outer zone of bio-UO₂ in a fashion reminiscent of that in UO_{2+x}, which surrounds a core of well-ordered stoichiometric UO_{2.00} (14).

Hence, if surface U(VI) is controlling UO₂ dissolution, then carbonate will play a major role in U immobilization and subsurface transport. By simulating a moderate DIC concentration representative of groundwater, dissolution rates of bio-UO₂ and dissolved U concentrations increased by 3 orders of magnitude compared to carbonate-free anoxic water. When applying the measured dissolution rates to field conditions, interactions of bio-UO₂ with other groundwater constituents including organic matter, Ca, Mg, Fe, and Mn must also be considered. For instance, organic matter, including biomass produced by the bacteria, may coat the bio-UO₂ particles and consume oxidants, thus retarding the oxidative dissolution of UO₂. The formation of ternary U(VI)-CO₃-Ca/Mg complexes in the system (32) can increase the stability of U(VI), and cations may adsorb on the bio-UO₂ particles and modify their solubility and dissolution kinetics. Analogous to Fe(III) (hydr)oxides (10), microbially generated Mn(III/IV) oxides may in turn oxidize UO₂ and thus decrease the stability of bio-UO₂ (33). Despite this increased environmental complexity, the intrinsic properties of bio-UO₂ provide a strong basis for estimating the stability of such nanoparticulate materials. Taking into account the residence time of undisturbed groundwater on the order of decades or centuries (29), it can be expected that UO₂ dissolution in such waters will be controlled by thermodynamics rather than kinetics, in particular by the thermodynamics of U(VI) species. Thus, in order to control U mobility in the subsurface, strategies are required to maintain strictly reducing conditions, sustain active anaerobic microbial populations, or increase the structural stability of biogenic UO₂.

Acknowledgments

We thank Dan Schwarz and David Clark for providing synthetic UO_{2.00} material and helpful advice. We acknowledge help from Edgar Leslie and Steve Picker. We appreciate the comments from three anonymous reviewers. Funding was provided by the U.S. Department of Energy, Office of Basic Energy Sciences grant DE-FG02-06ER64227, through the linked grants 1027869 (SSRL), 1027833 (EPFL), and 1027834 (WU). Part of this research was carried out at the Stanford Synchrotron Radiation Laboratory, a national user facility operated by Stanford University on behalf of the U.S. DOE-OBER. Portions of this project were supported by the DOE-BER-funded SSRL Environmental Remediation Science Program and the DOE-BER and NIH-NCRR-funded SSRL Structural Molecular Biology Program. Work carried out at EPFL was funded in part by the Swiss NSF grant 20021-113784.

Supporting Information Available

Detailed description of material preparation, experimental setup, modeling approach, structural characterization, and thermodynamic calculations (including 6 figures and 2 tables). This material is available free of charge via the Internet at <http://pubs.acs.org>.

Literature Cited

- Janeczek, J.; Ewing, R. C. Dissolution and alteration of uraninite under reducing conditions. *J. Nucl. Mater.* **1992**, *190*, 157–173.
- Finch, R. J.; Ewing, R. C. The corrosion of uraninite under oxidizing conditions. *J. Nucl. Mater.* **1992**, *190*, 133–156.
- Lovley, D. R.; Phillips, E. J. P.; Gorby, Y. A.; Landa, E. R. Microbial reduction of uranium. *Nature* **1991**, *350*, 413–416.
- Lovley, D.; Phillips, E. J. P. Reduction of uranium by *Desulfovibrio desulfuricans*. *Appl. Environ. Microbiol.* **1992**, *58*, 850–856.
- Tebo, B. M.; Obratsova, A. Y. Sulfate-reducing bacterium grows with Cr(VI), U(VI), Mn(IV), and Fe(III) as electron acceptors. *FEMS Microbiol. Lett.* **1998**, *162*, 193–198.
- Lovley, D. R.; Phillips, E. J. P. Bioremediation of uranium contamination with enzymatic uranium reduction. *Environ. Sci. Technol.* **1992**, *26*, 2228–2234.
- Anderson, R. T.; Vrionis, H. A.; Ortiz-Bernad, I.; Resch, C. T.; Long, P. E.; Dayvault, R.; Karp, K.; Marutzky, S.; Metzler, D. R.; Peacock, A.; White, D. C.; Lowe, M.; Lovley, D. R. Stimulating the in situ activity of *Geobacter* species to remove uranium from the groundwater of a uranium-contaminated aquifer. *Appl. Environ. Microbiol.* **2003**, *69*, 5884–5891.
- Senko, J. M.; Istok, J. D.; Sufliya, J. M.; Krumholz, L. R. In-situ evidence for uranium immobilization and remobilization. *Environ. Sci. Technol.* **2002**, *36*, 1491–1496.
- U.S. EPA. National Primary Drinking Water Regulations; Radionuclides; Final Rule. 2000, 40 CFR Parts 9, 141, and 142. Fed. Regist. Vol. 65: 76707–76753.
- Ginder-Vogel, M.; Criddle, C. S.; Fendorf, S. Thermodynamic constraints on the oxidation of biogenic UO₂ by Fe(III) (hydr)oxides. *Environ. Sci. Technol.* **2006**, *40*, 3544–3550.
- Senko, J. M.; Kelly, S. D.; Dohnalkova, A. C.; McDonough, J. T.; Kemner, K. M.; Burgos, W. D. The effect of U(VI) bioreduction

- kinetics on subsequent reoxidation of biogenic U(IV). *Geochim. Cosmochim. Acta* **2007**, *71*, 4644–4654.
- (12) Wan, J. M.; Tokunaga, T. K.; Brodie, E.; Wang, Z. M.; Zheng, Z. P.; Herman, D.; Hazen, T. C.; Firestone, M. K.; Sutton, S. R. Reoxidation of bioreduced uranium under reducing conditions. *Environ. Sci. Technol.* **2005**, *39*, 6162–6169.
- (13) Suzuki, Y.; Kelly, S. D.; Kemner, K. M.; Banfield, J. F. Nanometre-size products of uranium bioreduction. *Nature* **2002**, *419*, 134–135.
- (14) Schofield, E.; Veeramani, H.; Sharp, J.; Suvorova, E.; Bernier-Latmani, R.; Mehta, A.; Stahlman, J.; Clark, D. L.; Conradson, S. D.; Webb, S.; Bargar, J. R. Structure of biogenic uraninite produced by *Shewanella oneidensis*, strain MR-1. *Environ. Sci. Technol.* **2008**. (accepted).
- (15) Röllin, S.; Spahiu, K.; Eklund, U. B. Determination of dissolution rates of spent fuel in carbonate solutions under different redox conditions with a flow-through experiment. *J. Nucl. Mater.* **2001**, *297*, 231–243.
- (16) Johnson, D. A.; Florence, T. M. Spectrophotometric determination of uranium(VI) with 2-(5-bromo-2-pyridylazo)-5-diethylaminophenol. *Anal. Chim. Acta* **1971**, *53*, 73–79.
- (17) Webb, S. M. SIXPack: a Graphical User Interface for XAS Analysis Using IFEFFIT. *Phys. Scr.* **2005**, *T115*, 1011–1014.
- (18) Ankudinov, A. L.; Ravel, B.; Rehr, J. J.; Conradson, S. D. Real-space multiple-scattering calculation and interpretation of x-ray absorption near-edge structure. *Phys. Rev. B Condensed Matter* **1998**, *58*, 7565–7576.
- (19) Guillaumont, R.; Fanghanel, T.; Fuger, J.; Grenthe, I.; Neck, V.; Palmer, D. A.; Rand, M. H. *Update on the Chemical Thermodynamics of Uranium, Neptunium, Plutonium, Americium and Technetium*; OECD Nuclear Energy Agency; Elsevier: Amsterdam, 2003.
- (20) Rai, D.; Felmy, A. R.; Ryan, J. L. Uranium(IV) hydrolysis constants and solubility product of $\text{UO}_2 \cdot x\text{H}_2\text{O}(\text{am})$. *Inorg. Chem.* **1990**, *29*, 260–264.
- (21) Neck, V.; Kim, J. I. Solubility and hydrolysis of tetravalent actinides. *Radiochim. Acta* **2001**, *89*, 1–16.
- (22) Fanghanel, T.; Neck, V. Aquatic chemistry and solubility phenomena of actinide oxides/hydroxides. *Pure Appl. Chem.* **2002**, *74*, 1895–1907.
- (23) dePablo, J.; Casas, I.; Gimenez, J.; Marti, V.; Torrero, M. E. Solid surface evolution model to predict uranium release from unirradiated UO_2 and nuclear spent fuel dissolution under oxidizing conditions. *J. Nucl. Mater.* **1996**, *232*, 138–145.
- (24) Gimenez, J.; de Pablo, J.; Torrero, M. E.; Casas, I. Conceptual and mathematical model for the $\text{UO}_{2(\text{s})}$ dissolution in brines under different redox conditions. *Radiochim. Acta* **1997**, *78*, 21–25.
- (25) Pierce, E. M.; Icenhower, J. P.; Serne, R. J.; Catalano, J. G. Experimental determination of $\text{UO}_{2(\text{cr})}$ dissolution kinetics: Effects of solution saturation state and pH. *J. Nucl. Mater.* **2005**, *345*, 206–218.
- (26) Christensen, H.; Sunder, S.; Shoemith, D. W. Oxidation of nuclear fuel (UO_2) by the products of water radiolysis: development of a kinetic model. *J. Alloys Compd.* **1994**, *213/214*, 93–99.
- (27) Suzuki, T.; Abdelouas, A.; Grambow, B.; Mennecart, T.; Blondiaux, G. Oxidation and dissolution rates of $\text{UO}_{2(\text{s})}$ in carbonate-rich solutions under external alpha irradiation and initially reducing conditions. *Radiochim. Acta* **2006**, *94*, 567–573.
- (28) Kubatko, K. A. H.; Helean, K. B.; Navrotsky, A.; Burns, P. C. Stability of peroxide-containing uranyl minerals. *Science* **2003**, *302*, 1191–1193.
- (29) Bruno, J.; Casas, I.; Puigdomenech, I. The Kinetics of Dissolution of UO_2 under Reducing Conditions and the Influence of an Oxidized Surface-Layer (UO_{2+x}) - Application of a Continuous Flow-through Reactor. *Geochim. Cosmochim. Acta* **1991**, *55*, 647–658.
- (30) Lasaga, A. C. Fundamental approaches in describing mineral dissolution and precipitation rates. In *Chemical Weathering Rates of Silicate Minerals*; White, A. F., Brantley, S. L., Eds.; Mineralogical Society of America: Washington, DC, 1995; Vol 31, pp 23–86.
- (31) Stumm, W.; Morgan, J. J. *Aquatic Chemistry*, 3rd ed.; John Wiley & Sons, Inc.: New York, 1996.
- (32) Dong, W. M.; Brooks, S. C. Determination of the formation constants of ternary complexes of uranyl and carbonate with alkaline earth metals (Mg^{2+} , Ca^{2+} , Sr^{2+} , and Ba^{2+}) using anion exchange method. *Environ. Sci. Technol.* **2006**, *40*, 4689–4695.
- (33) Chinni, S.; Anderson, C.; Ulrich, K.-U.; Giammar, D. E.; Tebo, B. M. Indirect UO_2 oxidation by Mn(II)-oxidizing spores of *Bacillus* sp. strain SG-1 and the effect of U and Mn concentrations. *Environ. Sci. Technol.* 2008. (submitted).
- (34) Frazier, S. W.; Kretzschmar, R.; Kraemer, S. M. Bacterial siderophores promote dissolution of UO_2 under reducing conditions. *Environ. Sci. Technol.* **2005**, *39*, 5709–5715.

ES800647U